Phase retrieval for hard X-ray computed tomography of samples with hybrid compositions

Huiqiang Liu (刘慧强)[1], Yuqi Ren (任玉琦)[1], Han Guo (郭 瀚)[1], Yanling Xue (薛艳玲)[1], Honglan Xie (谢红兰)[1], Tiqiao Xiao (肖体乔)[1*], and Xizeng Wu (吴希增)[2]**

[1]*Shanghai Institute of Applied Physics, Chinese Academy of Sciences, Shanghai 201204, China*

[2]*Department of Radiology, University of Alabama at Birmingham, Birmingham, Alabama 35233, USA*

[*]*Corresponding author: tqxiao@sinap.ac.cn;* [**]*corresponding author: xwu@uabmc.edu*

Received May 31, 2012; accepted June 20, 2012; posted online September 14, 2012

X-ray tomography of samples containing both weakly and strongly absorbing materials are necessary in material and biomedical imaging. Extending the validity of the phase-attenuation duality (PAD) method, the propagation-based phase-contrast computed tomography (PPCT) of a sample with hybrid compositions of both the light and dense components with 60 keV of synchrotron radiation is investigated. The experimental results show that the PAD-based PPCT is effective in imaging both the weakly and strongly absorbing components simultaneously. Compared with the direct PPCT technique, the PAD-based PPCT technique demonstrates its excellent capability in material discrimination and characterization. In addition, the PAD-based PPCT exhibits a striking performance on the image contrast enhancement and noise suppression. Therefore, this technique is useful for material and biomedical imaging applications, especially when the radiation dose involved imposes a serious constraint.

OCIS codes: 110.6960, 100.5070, 170.3010, 340.7440.

doi: 10.3788/COL201210.121101.

X-ray tomography of samples containing both weakly and strongly absorbing materials is necessary in material and biomedical imaging[1,2]. Propagation-based phase-contrast computed tomography (PPCT) is a good choice for this purpose because it utilizes highly sensitive phase contrast and requires a relatively simple setup[3−5]. Two different types of approaches are available for PPCT. One type is direct PPCT, in which the tomographic reconstruction, such as that based on the filtered back-projection (FBP) algorithm, is directly applied to the acquired angular projections with mixed attenuation and phase contrast. The other type is phase retrieval-based PPCT, in which the acquired projections are preprocessed with the phase retrieval before tomographic reconstruction. The phase retrieval on the acquired angular projections can enhance image contrast, reduce artifacts, and enable quantitative characterization of the sample[6−8]. However, multiple sets of projections must be obtained at different sample-detector distances (SDDs) to proceed with the phase retrieval, indicating that a laborious acquisition process is needed, and considerably more radiation dose is introduced[9−11]. Therefore, a phase retrieval-based PPCT method that uses only a single set of projections is highly desirable.

The phase shift results from X-ray coherent scattering, whereas the attenuation arises from the three kinds of interactions between X-ray and matter, such as photoelectric absorption, incoherent scattering, and coherent scattering. The phase attenuation duality (PAD) relation holds for X-rays of 60–500 keV transmitted from the samples of light elements with atomic numbers $Z < 10$[7]. In these cases, the attenuations and phase shifts of the samples are all related to the projected electron densities along the X-ray paths. Under PAD conditions, the X-ray intensity propagation equation is simplified, such that robust phase retrieval can be achieved from only a single projection at each view angle. This letter reports the experimental results for a sample with hybrid composition to demonstrate the capability of the PAD-based PPCT technique in material discrimination and characterization.

A sample for phase-contrast imaging is modeled as a 2D transmission function in the object plane $\mathrm{X}=(x,\ y)$, with the amplitude denoted by $A(\mathrm{X})$ and the phase by $\varphi(\mathrm{X})$. Maps $A^2(\mathrm{X})$ and $\varphi(\mathrm{X})$ are the attenuation image of the sample and the phase image, respectively. $A^2(\mathrm{X})$ is related to the projected electron density $\rho_{\mathrm{e,\,p}}(\mathrm{X})$ when the PAD condition is satisfied, given that $A^2(\mathrm{X})=\exp[-\sigma_{\mathrm{KN}}\rho_{\mathrm{e,\,p}}(\mathrm{X})]$, where σ_{KN} is the total cross section of the X-ray Compton scattering from a single free electron. However, the phase shift $\varphi(\mathrm{X})$ along a ray path is given by $\lambda r_{\mathrm{e}}\rho_{\mathrm{e,\,p}}(\mathrm{X})$, and r_{e} is the classic electron radius. Based on the paraxial Fresnel-Kirchhoff diffraction, the projected electron density $\rho_{\mathrm{e,\,p}}(\mathrm{X})$ is given as[7]

$$\rho_{\mathrm{e,p}}(\mathrm{X})=-\frac{1}{\sigma_{\mathrm{KN}}}\ln\left\{f^{-1}\left\{\frac{f\left\{M^2I\left(M\mathrm{X};R_1+R_2\right)\right\}}{I_{\mathrm{in}}\left(1+2\pi\left(\frac{\lambda^2r_{\mathrm{e}}R_2}{M\sigma_{\mathrm{KN}}}\right)u^2\right)}\right\}\right\}, \tag{1}$$

where $M=(R_1+R_2)/R_1$, R_1 is the source-to-sample distance, R_2 denotes the SDD, $I(\mathrm{X};R_1+R_2)$ is the projection intensity at detector plane, and I_{in} is the entrance intensity. In Eq. (1), $f\{\ \}$ denotes the 2D Fourier transform, $f^{-1}\{\ \}$ is its inverse, and u denotes the spatial frequency vector in the object plane. The initial angular projections in PAD-based PPCT are preprocessed with PAD-based phase retrievals, and then the standard FBP algorithm is employed to reconstruct the distribution of the electron densities in the sample from the preprocessed projections.

The experiments were performed at the X-ray Imaging and Biomedical Application Beamline (BL13W1) of the

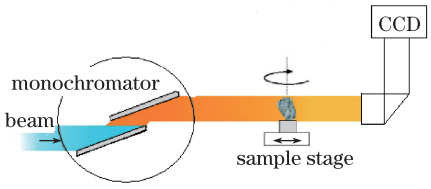

Fig. 1. Schematic of the propagation-based imaging system.

Shanghai Synchrotron Radiation Facility (SSRF), which can provide high flux X-rays in the energy range of 8–72.5 keV. The sample was located at approximately 34-m downstream of the wiggler source to provide both high spatial coherence and almost parallel beam. The schematic of the experimental setup is demonstrated in Fig. 1. The experiments were conducted at 60 keV, with a SDD of 80 cm. The phantom for the experiments was composed of four types of standard materials (GoodFellow Cambridge Limited), namely, an alumina rod (Al_2O_3, $\Phi = 1$ mm, 3.9 g/cm^{-3}), an aluminum tube (Al, $\Phi_{\rm in}$= 1.166 mm, $\Phi_{\rm out}$= 1.42 mm, 2.7 g/cm^{-3}), a PTFE tube (C_2F_4, $\Phi_{\rm in} = 1$ mm, $\Phi_{\rm out}$= 1.82 mm, 2.2 g/cm^{-3}), and a PMMA rod ($C_5H_8O_2$, $\Phi = 1$ mm, 1.19 g/cm^{-3}). The metallic oxide and metal components were chosen to simulate dense materials, such as the bones, whereas the polymer components were used to simulate light materials, such as soft tissues.

A total of 900 phase-contrast radiographs were collected over a 180° rotation for a tomographic data set; each radiograph was acquired with an exposure time of 208 ms. The detector was a CCD (Photonic Science) with a 9-μm effective pixel size. Considering that a highly coherent X-ray beam and large SSD were employed, all these radiographs exhibited not only the usual attenuation-based image contrast, but also enhanced material interfaces as a result of the refraction and diffraction of the phase-shifted X-rays. For comparison, tomograms were reconstructed using the angular projection data set through two different techniques, namely, the direct and the PAD-based PPCTs. The tomogram by direct PPCT, in which the standard FBP algorithm was directly applied to the initial projections, is shown in Fig. 2(a). The structures for the dense and light material components can all be distinguished from each other because of the edge enhancements at the interfaces. Notably, some micropores inside the Al_2O_3 rod became apparent as the results of the edge-enhancement. This feature indicates that the direct PPCT method is suitable for distinguishing the small cracks or voids embedded inside a sample. However, the bulk contrast between the different materials appeared rather weak. Moreover, Fig. 2(a) presents anomalously large or even negative apparent linear attenuation coefficients at material interfaces, impeding proper material characterization. According to a general analysis of the direct PPCT technique, the pixel value indicated in Fig. 2(a), namely the reconstructed apparent attenuation coefficient, was not equal to the material linear attenuation coefficient. Rather, the reconstructed apparent attenuation coefficient is a sum of three parts, i.e., the linear attenuation coefficient of the material, the Laplacian of the refractive index of the material, and the nonlocal contribution, which is dependent on the global variations in the phantom attenuation coefficients and refractive indices[5]. The presence of an excessive noise added uncertainty to the apparent attenuation coefficients.

The tomogram shown in Fig. 2(b) was reconstructed using the PAD-based PPCT method, in which the acquired projections were preprocessed with the PAD-based phase retrievals to retrieve the $\rho_{\rm e,\ p}$-maps for each individual angular view. FBP-based algorithm was then applied to these retrieved $\rho_{\rm e,\ p}$-maps for tomography reconstruction. For comparison, the intensity profiles along two white dash-dot circles in Figs. 2(a) and (b) are shown in Fig. 3. The red dashed line associated with the direct PPCT method shows severe high-frequency noise and weak bulk contrast, which cannot provide useful means for material characterization. However, the blue solid line with the PAD-based PPCT method demonstrates good bulk-contrast and high signal-to-noise ratios, enabling qualitative and quantitative material characterization. The bulk contrast-to-noise ratios (CNRs) achieved in Figs. 2(a) and (b) were compared to quantify the noise-suppression advantage of the PAD-based PPCT. The signal was defined as the mean image intensity in a region of interest, excluding the boundaries. The contrast was defined as the difference in the signals in two regions of interest, and the noise was the average of the standard deviations of the intensities in the two regions. The bulk CNRs achieved with the two techniques are shown in Fig. 4, indicating that the bulk CNRs with the PAD-based PPCT method were approximately 10 to 15 times higher than that with the direct PPCT method. This significant enhancement in the bulk CNR implies that the PAD-based method has the potential to reduce tremendously the radiation dose. This feature is particularly useful for biomedical applications, where a good bulk contrast is critical for tissue/lesion characterization. Some ring artifacts are present in both Figs. 2(a) and (b), which are due to the beam quality degradation at high photon energies.

In addition, the histograms derived from Figs. 2(a) and (b) are demonstrated in Figs. 5(a) and (b), respectively. Figure 5(a), which is derived from direct PPCT, shows that the overlapped histogram peaks hamper the discrimination between the four different materials in the sample. However, Fig. 5(b) from the PAD-based PPCT shows that the well-separated peaks clearly discriminate among the four different materials in the sample. The histogram peaks in Fig. 5(b) were identified as those of PMMA, PTFE, Al, and Al_2O_3 from left to right.

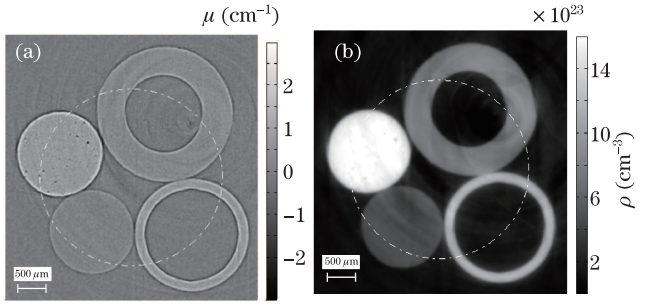

Fig. 2. Reconstructions for the sample at 60 keV. Tomograms of (a) direct and (b) PAD-based PPCTs.

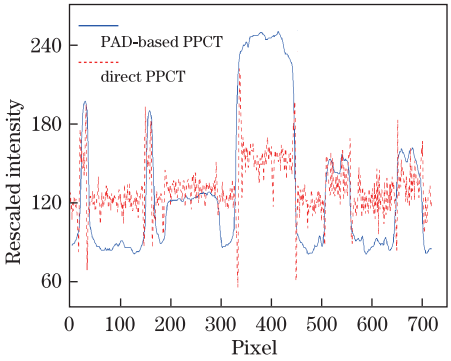

Fig. 3. (Color online) Profiles of rescaled intensity on the trace of white dash-dot circle in Figs. 2(a) and (b), respectively.

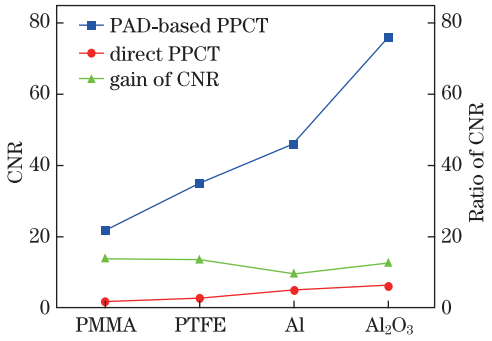

Fig. 4. Plots of CNR for both direct and PAD-based PPCTs as well as the gain of the CNRs of the PAD-based and direct PPCTs.

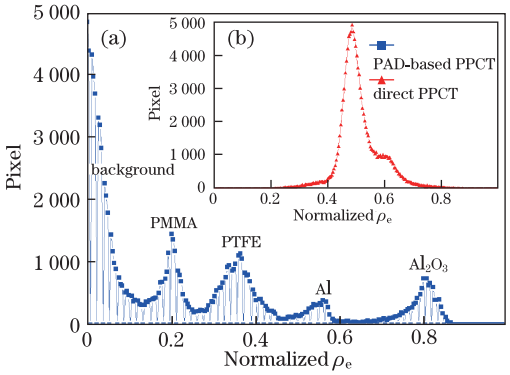

Fig. 5. Histograms of the electron density distribution of the samples with (a) direct and (b) PAD-based PPCTs.

This layout of the peaks is consistent with the true electron density values of these materials.

Moreover, some quantitative information can also be obtained from the histogram shown in Fig. 5(b). The PAD condition at 60 keV holds for the materials made of light elements with Z<10. Hence, good accuracies can be achieved in recovering the electron densities of the PTFE tube and PMMA rod in the sample because these two materials consist of the light elements with Z<10. The electron density of a material is theoretically expressed as $\rho_e = N_a \rho \sum[w_i(Z_i/A_i)]$, where N_a is the Avogadro constant and ρ is the mass density of the material; w_i, Z_i, and A_i are the elemental weight fraction, atomic number, and atomic weight of the material, respectively. Therefore, the obtained theoretical electron density values were ρ_e(PMMA) = 3.865×10^{23} cm^{-3} and ρ_e(PTFE) = 6.358×10^{23} cm^{-3}, and their ratio was ρ_e(PTFE)/ρ_e(PMMA)=1.645. However, the histogram in Fig. 5(b) shows that the ratio $[\rho_e(\text{PTFE})/\rho_e(\text{PMMA})]_{\text{peak}}$ = 1.714 differs from its theoretical value by only 4.2%. Moreover, Fig. 2(b) shows that the reconstructed electron density values of these two materials are less than 12% different from their theoretical values. These results demonstrate that the PAD-based PPCT method achieved good accuracies in evaluating the electron densities of the materials composed of light elements. Similar ratios involving aluminum atoms, such as $[\rho_e(\text{Al})/\rho_e(\text{PMMA})]_{\text{peak}}$ and $[\rho_e(\text{Al}_2\text{O}_3)/\rho_e(\text{PMMA})]_{\text{peak}}$, differ from their theoretical ratios by as much as 36%. These larger errors are expected considering that the PAD does not hold for heavier elements, such as aluminum (Z=13). These errors associated with heavier elements can be reduced as the X-ray photon energy increases.

Although several other methods that use only a single set of projections for the phase retrieval-based PPCT are available, these methods are not applicable to samples of hybrid materials with both light and dense components. As analyzed in Ref. [13], some of these methods require samples with diminished attenuation, whereas others are applicable only to samples composed of single or binary materials with known linear attenuation coefficients and refractive indices. The proposed method is therefore advantageous because it does not require such assumptions and constraints. The PAD-assumption holds only if the X-ray Compton scattering dominates in the X-ray attenuation process, as we point out at the beginning. Hence, additional research is needed to investigate whether the PAD-based PPCT method is applicable for other combinations of light and dense materials encountered in material and biomedical applications.

In conclusion, extending the validity of the PAD-based method, the PPCT of a sample with hybrid compositions is investigated using a 60-keV synchrotron radiation. The experimental results show that the PAD-based PPCT is effective in imaging simultaneously both the weakly and strongly absorbing components. Compared with the direct PPCT technique, the PAD-based PPCT demonstrats its excellent capability in material discrimination and characterization. This PAD-based method also exhibits a striking performance on the bulk-contrast enhancement and noise suppression. This technique therefore has great potential for material and biomedical applications, especially when the radiation dose involved imposes a serious constraint.

This work was supported by the National Basic Research Program of China (No. 2010CB834301), the External Cooperation Program of Chinese Academy of Science (No. GJHZ09058), and the National Natural Science Foundation of China (No. 11105213). XW was supported in part by the U.S. NIH grant R01CA142587 and the DoD Breast Cancer Research Program award W81XWH-08-1-0613.

References

1. P. Cloetens, R. Mache, M. Schlenker, and S. Lerbs-Mache, PNAS **103,** 14626 (2006).
2. J. P. Guigay, M. Langer, R. Boistel, and P. Cloetens, Opt. Lett. **32,** 1617 (2007).
3. P. Cloetens, W. Ludwig, J. Baruchel, D. Van Dyck, J. Van Landuyt, J. P. Guigay, and M. Schlenker, Appl. Phys. Lett. **75,** 2912 (1999).
4. R. Chen, H. Xie, L. Rigon, R. Longo, E. Castelli, and T. Xiao, Opt. Lett. **36,** 1719 (2011).
5. X. Wu, H. Liu, and A. Yan, EJR **68S,** S8 (2008).
6. M. Langer, P. Cloetens, and F. Peyrin, IEEE Trans. Image Process. **19,** 2428 (2010).
7. X. Wu, H. Liu, and A. Yan, Opt. Lett. **30,** 379 (2005).
8. A. Groso, R. Abela, and M. Stampanoni, Opt. Express **14,** 8103 (2006).
9. M. Langer, P. Cloetens, J. P. Guigay, and F. Peyrin, Med. Phys. **35,** 4556 (2008).
10. A. Burvall, U. Lundström, P. A. C. Takman, D. H. Larsson, and H. M. Hertz, Opt. Express **19,** 10359 (2011).
11. Y. Ren, C. Chen, R. Chen, G. Zhou, Y. Wang, and T. Xiao, Opt. Express **19,** 4170 (2011).